THE JOURNAL OF PHYSICAL CHEMISTRY A
A JOURNAL OF THE AMERICAN CHEMICAL SOCIETY

pubs.acs.org/JPCA Article

Time-Domain Vibrational Action Spectroscopy of Cryogenically Cooled, Messenger-Tagged Ions Using Ultrafast IR Pulses

Liangyi Chen, Jessika L. S. Dean, and Joseph A. Fournier*

Cite This: J. Phys. Chem. A 2021, 125, 10235−10244 Read Online

ACCESS | Metrics & More | Article Recommendations | Supporting Information

ABSTRACT: Herein, we present the initial steps toward developing a framework that will enable the characterization of photoinitiated dynamics within large molecular ions in the gas phase with temporal and energy resolution. We combine the established techniques of tag-loss action spectroscopy on cryogenically trapped molecular ions with ultrafast vibrational spectroscopy by measuring the linear action spectrum of N_2-tagged protonated diglycine ($GlyGlyH^+{\cdot}N_2$) with an ultrafast infrared (IR) pulse pair. The presented time-domain data demonstrate that the excited-state vibrational populations in the tagged parent ions are modulated by the ultrafast IR pulse pair and encoded through the messenger tag-loss action response. The Fourier transform of the time-domain action interferograms yields the linear frequency-domain vibrational spectrum of the ion ensemble, and we show that this spectrum matches the linear spectrum collected in a traditional manner using a frequency-resolved IR laser. Time- and frequency-domain interpretations of the data are considered and discussed. Finally, we demonstrate the acquisition of nonlinear signals through cross-polarization pump−probe experiments. These results validate the prerequisite first steps of combining tag-loss action spectroscopy with two-dimensional IR spectroscopy for probing dynamics in gas-phase molecular ions.

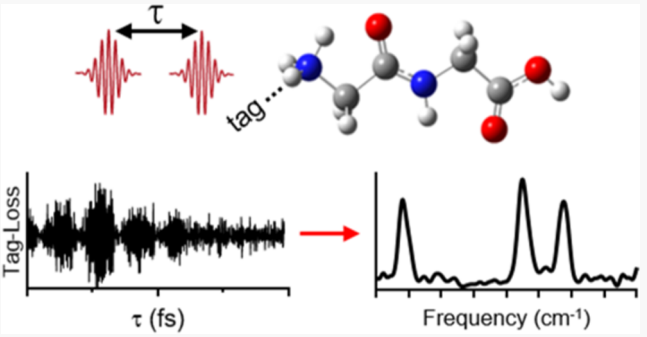

INTRODUCTION

Experimental and technological advances throughout the spectroscopy and chemical physics communities have led to the rapid development of new methods for increasingly detailed investigations of molecular structures, interactions, and dynamics. Condensed-phase ultrafast spectroscopies can now readily interrogate dynamics on time scales that reveal nuclear motions along reaction pathways. In particular, coherent multidimensional spectroscopies such as two-dimensional infrared (2D IR),[1,2] 2D electronic (2D ES),[3,4] 2D THz,[5] and mixed methods[6,7] have emerged as powerful methods to extract structural and dynamical information that are not readily obtainable from linear optical spectra, such as resolving homogeneous vs. inhomogeneous line broadening contributions and cross peaks, which indicate molecular coupling or transformations. Despite these advances and impressive volume and scope of research, there remain key limitations in condensed-phase multidimensional spectroscopies including high sample concentrations, broad transitions, spectral congestion, solvent background, solvent-molecule dynamics and coupling, and, most critically, interpretational difficulties that are not easily addressed with current computational approaches.

Ultrafast multidimensional spectroscopies of dilute gas-phase systems could alleviate many of the challenges faced in the condensed phase while providing stringent benchmarks for computational methods and experimental models to aid in the interpretation of condensed-phase measurements. There are some problems with performing nonlinear spectroscopies on gas-phase species which must be overcome or addressed. In particular, sample densities in solution tend to be significantly higher than in the gas phase such that direct measurement of light absorption is generally not possible for dilute gas-phase ensembles. Measurement of light absorption must be done indirectly through action schemes such as photoionization or photofragmentation. Importantly, excited-state populations and nonlinear responses induced by broad-band ultrafast pulse sequences must be mapped by the indirect action response observable.

Thirty years ago, Scherer et al. measured modulations in the fluorescence emitted from the B-state of photoexcited I_2 as a function of the time delay between two replica ultrafast pulses.[8] The Fourier transform of the time-domain fluorescence action signal yielded a progression of transitions consistent with the vibrational frequencies of B-state I_2. The excited-state populations were, then, directly proportional to the measured

Received: March 5, 2021
Revised: November 4, 2021
Published: November 17, 2021

https://doi.org/10.1021/acs.jpca.1c01996
J. Phys. Chem. A 2021, 125, 10235−10244

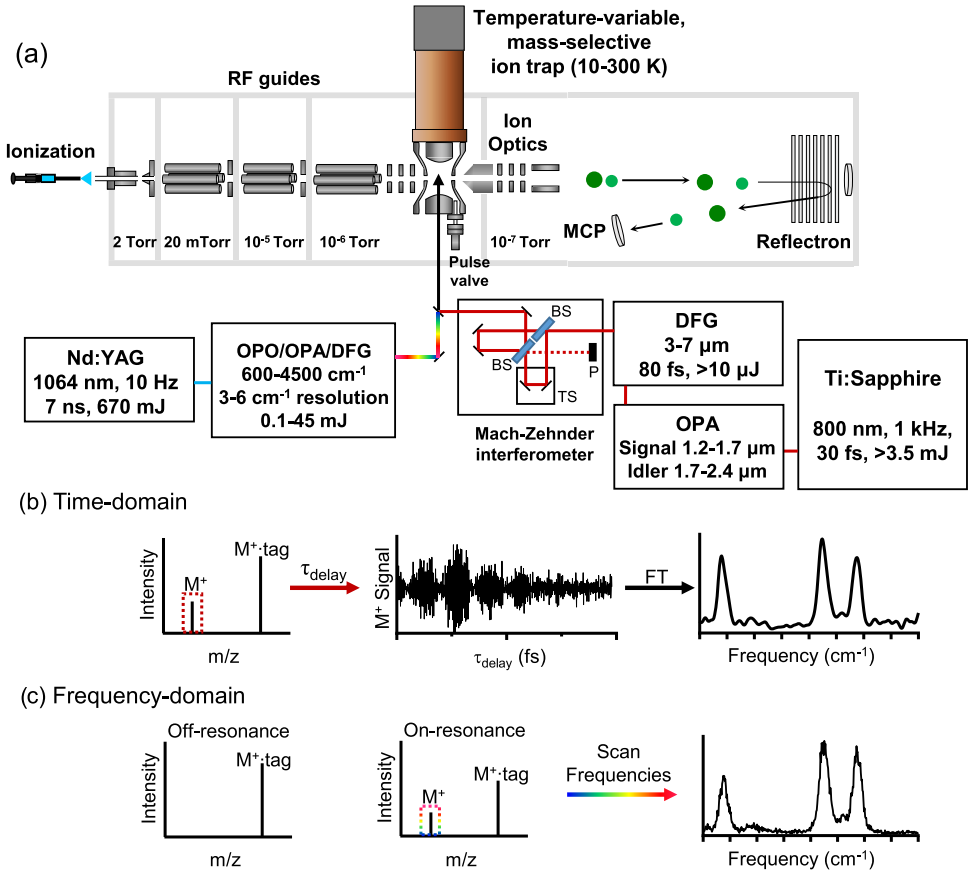

Figure 1. (a) Schematic of the photofragmentation mass spectrometer. Electrosprayed ions are stored and messenger-tagged in a cryogenically cooled, mass-selective Paul trap. After mass selection, the tagged ions are photoexcited directly in the ion trap. Tagged parent ions and untagged photofragment daughter ions are separated in a time-of-flight reflectron mass spectrometer. (b) Time-domain experiments utilize an ultrafast IR pulse pair to monitor the modulation in the photofragment yield as a function of the time delay between the pulse pair. The pulse pair is generated in a Mach−Zehnder interferometer. BS: beamsplitter; TS: translation stage; P: power meter for active monitoring of the dark arm (dashed line). The Fourier transform of the time-domain signal gives the linear vibrational action spectrum. (c) Frequency-domain experiments utilize a tunable IR source to monitor the photofragment yield as a function of laser frequency.

fluorescence yield as a function of the pulse pair delay time. More relevant to the present study, over a decade ago, Marcus obtained 2D ES spectra of Rb vapor by monitoring intensity modulations in the emitted fluorescence as a function of the delay times between a series of four ultrafast pulses.[9,10] Recently, the groups of Brixner (NO_2)[11] and Stienkemeier (Rb dimer and trimer trapped in He nanodroplets)[12,13] have reported the first gas-phase 2D ES spectra of neutral molecules by monitoring time-domain modulations in photoionization and/or ionic photofragmentation yields detected with mass spectrometry. Action detection methods have also been employed in the condensed phase with Cundiff demonstrating the collection of 2D ES spectra of semiconductor nanowires by monitoring modulation in photocurrent[14] and van Hulst measuring transient absorption spectra of a single molecule through fluorescence modulation.[15] In related studies, Allison has demonstrated the collection of electronic pump−probe transient absorption spectra on neutral gas-phase molecules and clusters via direct absorption measurements using cavity-enhancement techniques employing high repetition rate frequency-comb lasers.[16,17] These important experiments have set the precedent for obtaining ultrafast multidimensional spectra in the gas phase using action-based detection schemes.

Two critical next steps are extending these techniques to molecular ions and into the infrared region. Compared to neutrals, the versatility of mass spectrometric methods affords much greater experimental control by allowing for the composition-selected preparation of the desired chemical species. Soft ionization techniques like electrospray ionization now allow for the isolation of increasingly complex and diverse systems extracted from solution that are not generally accessible with neutral techniques, from host−guest complexes,[18−20] to catalysts and their intermediates,[21−24] to nanoparticles,[25] to complex cluster systems.[26−31] Linear action spectra of molecular ions are often collected using the messenger-tagging method,[32] where gas adducts (H_2, N_2, Ar) form weakly bound complexes with the ion of interest through buffer gas collisions in cryogenically cooled ion traps[33,34] or within supersonic expansions.[35] In a typical experiment, a high-frequency-resolution laser is scanned through the optical wavelengths of interest and the amount of tag-loss photofragmentation is measured as a function of laser frequency to record the linear action spectrum.[30,36,37] Importantly, messenger tag loss occurs in the single-photon regime. Further, cryogenic cooling enables the lowering or stabilization of molecular ions into the lowest-energy conformers/isomers. The low sample temperatures (<50 K) result in populations only in the lowest vibrational and, to some extent, rotational levels. Consequently, highly resolved frequency-domain linear

https://doi.org/10.1021/acs.jpca.1c01996
J. Phys. Chem. A 2021, 125, 10235−10244

spectra can be obtained that are directly comparable with theoretical predictions.

Here, we report a method for collecting frequency-resolved linear vibrational action spectra of gaseous, messenger-tagged molecular ions measured in the time domain using an ultrafast IR pulse pair. The system chosen for this demonstration is N_2-tagged protonated diglycine, $GlyGlyH^+ \cdot N_2$, which has been extensively studied using high-frequency-resolution cryogenic ion vibrational spectroscopy (CIVS) by Johnson.[38−41] We focus on the amide I and II vibrations, a spectral region that has proven highly fruitful in the condensed-phase 2D IR community. $GlyGlyH^+$, therefore, presents itself as an ideal test system. We observe strong modulation of the messenger tag-loss action signal as a function of the pulse pair delay time that persists for >1.5 ps. Fourier transformation of the measured time-domain tag-loss signal yields the linear vibrational spectrum of the ion ensemble and matches that collected using standard high-frequency-resolution IR sources. We discuss the observed time-domain signal in terms of both time- and frequency-domain interpretations. Further, we demonstrate the measurement of weaker nonlinear signals using cross-polarized pulses where the background two-pulse linear response is eliminated. Importantly, the results lay the foundation for the collection of ultrafast time-resolved and multidimensional action spectra of tagged molecular ions and we discuss the prospects of such experiments.

EXPERIMENTAL SECTION

Apparatus. A schematic of the experimental apparatus is shown in Figure 1. The homebuilt photofragmentation mass spectrometer is similar in design to those of Johnson[42] and Garand.[43] Ions are generated via electrospray ionization by applying 3−5 kV to a 34-gauge stainless steel capillary housed in a Thermo LCQ ESI source, which is secured to an Al block that houses a 0.030 in. ID, 1/16 in. OD, 3.9 in. long stainless steel capillary inlet. Generated ions are transferred via the capillary inlet to the first differentially pumped stage (2 Torr) and skimmed by a 0.030 in. nose cone. The ions are guided in the second differential stage (20 mTorr) by an RF-only hexapole (2 MHz, 500 V_{pp}). A 0.060 in. aperture leads to the third differentially pumped stage (<1×10^{-5} Torr) and a second RF-only hexapole guide (2 MHz, 300 V_{pp}). A custom-designed gate valve (Ardara Technologies) separates the source region from the ion trap and detection regions. The thin (0.1 in.) gate minimizes the separation (0.150 in.) between the second and third hexapole (2 MHz, 300 V_{pp}) guides allowing for efficient ion transfer. All hexapole guides have rod diameters of 3/16 in. and an assembled inscribed diameter of 0.372 in. The RF (model PSRF-128) and electrospray (PS_ESI_CONT_139) power supplies were purchased from Ardara Technologies. Following the third hexapole guide, the ions are focused by einzel lenses into a 3D quadrupole Paul trap (Jordan TOF) attached to the second stage of a closed-cycle helium cryostat (Janis Research; SHI-4−15-HV). Buffer gas is introduced into the trap through a pulse valve (Parker Hannifin; Series 9 general valve) attached to an Al heat shield that encloses the trap. The pulse valve is thermally isolated from the Al heat shield, which is attached to the Au-plated heat shield enclosing the 50 K first stage of the cryostat, with a small length of Teflon tubing. A 1200 L/s turbomolecular pump attached to the trap chamber allows for sufficient evacuation of the pulsed buffer gas during experiments. Background pressure in this region is 3×10^{-7} Torr and increases to $1−3 \times 10^{-6}$ Torr during experiments. The pressure inside the trap is estimated to be a few mTorr.[44] Ions are extracted from the trap into a reflectron time-of-flight (TOF) mass spectrometer and detected with a dual MCP detector (Jordan TOF). Pressure in the TOF and detection region is 2×10^{-7} Torr.

Methods. *Ion Preparation.* Electrosprayed ions were generated from a 300 to 500 μM solution of diglycine in methanol with approximately 10 ppm of formic acid. Generated $GlyGlyH^+$ ions were initially stored in the first hexapole guide for approximately 95 ms by applying a repelling voltage to the aperture. In the following cycle, the stored ions were released 1 ms after the pulse valve fired to maximize trapping efficiency. The short distance between the pulse valve and trap yields an ∼35 ms burst of gas that enables sufficient evacuation of background gas from the trap prior to laser excitation and ion ejection. In the experiments described here, the cryostat temperature was held at 28 K allowing for the condensation of N_2 tags onto the $GlyGlyH^+$ parent ions. The buffer gas was He (10 psi backing pressure) with the N_2 coming from trace impurities (<1%). The trap float, RF amplitude, and buffer gas pressure were optimized for the production of a single N_2 adduct. The estimated ion density is $\sim 10^6$ cm^{-3}. After 20 ms of trapping, a low voltage (∼4 V_{pp}) RF pulse was applied (Stanford Research System; DS345) to the trap entrance electrode and tuned to the secular frequency of the untagged parent ion for approximately 5 ms. This RF pulse sweeps the untagged parent ion out of the trap.[45] After 95 ms of storage in the trap, the trap RF is clamped off and the exit electrode is pulsed to −400 V to extract the ions out of the trap. Extraction optics are floated at −1500 V to accelerate the ions into the TOF region. The estimated number of tagged ions detected per cycle is estimated to be $\sim 10^4−10^5$.

Time-Domain Experiments. The compressed output of a Ti:sapphire oscillator/regenerative amplifier system (Coherent Astrella, 800 nm, 1 kHz, 35 fs, 3.6 mJ/pulse) pumps a commercial OPA (Light Conversion TOPAS Prime) generating tunable near-IR signal (1.2−1.7 μm) and idler (1.7−2.4 μm) pulses. The signal and idler outputs are difference-frequency mixed in a type I $AgGaS_2$ crystal (Eksma Optics; AGS-802H) in a homebuilt source to generate tunable IR pulses[46] (3−7 μm, >10 μJ/pulse, >200 cm^{-1} full-width half-maximum (FWHM)). A pulse pair is generated in a Mach−Zehnder interferometer (MZI) consisting of two KBr beamsplitters (Spectral Systems; 945-0506H). The dark arm of the MZI is actively monitored with a power meter and used to phase-correct the spectra. The delay between the two pulses is controlled with a high-accuracy translation stage (AeroTech; ANT95L).

The IR pulse pair was softly focused into the trap using a −800 mm radius concave spherical mirror (400 mm focal length; laser focal diameter <1 mm) through a KBr window (International Crystal Laboratories; 0002D-262). The repetition rate of the ion trap/mass spectrometer was held at its typical value of 10 Hz (100 ms). This meant that approximately 80 ultrafast pulse pairs (1 kHz repetition rate, 1 ms) irradiated the ions during the ∼80 ms between the end of the sweeping pulse and ion ejection from the trap. Importantly, the 1 ms delay between successive ultrafast pulses means that tagged ions cannot be excited by multiple pulse pairs. Since tag loss occurs in the single-photon regime,[38] if an ion is excited by a pulse, the messenger tag will dissociate well before the next pulse pair. Further, since the trap is mostly

https://doi.org/10.1021/acs.jpca.1c01996
J. Phys. Chem. A 2021, 125, 10235−10244

evacuated of the He buffer gas during the first 20 ms before irradiation, recooling and retagging will not occur. Therefore, this scheme can be viewed as the accumulation of a tag-loss signal from 80 individual experiments during each mass spectrometry cycle. The fluence is estimated to be $\sim 10^2$ μJ/cm^2 per pulse (6 μJ/pulse) with a pulse width of 85 fs, as measured through interferometric autocorrelation. The spot size diameter of the pulse is about 1 mm, giving an excitation volume of $\sim 10^{-3}$ cm^3. Lowering the power of the ultrafast pulses by half decreased the tag-loss photofragmentation by half and resulted in similar time- and frequency-domain spectra (Supporting Information Figure S1). These observations, along with calculations presented in the Discussion section, suggest that the ultrafast experiments were performed in the linear regime.

Photofragmentation yield was monitored by recording the intensities of the tag-loss daughter ion and tagged parent ion (Picoscope; 5243D) as a function of the pulse pair delay time. Data was collected in 5 fs steps from −500 fs to 5000 fs to sufficiently sample the interferogram, resulting in a resolution of about 7 cm^{-1}. For each delay time, the signal was averaged over 5−20 cycles of the mass spectrometer depending on signal stability. For averaging over 10 mass spectrometer cycles, a single scan took approximately 30 min to collect. A total of 15 interferograms were collected during four separate days. Each individual interferogram was phase-corrected with the Mertz method[47] using the output of the dark arm of the MZI, which was recorded simultaneously with the photofragmentation signal. The frequency-domain spectrum was then inverse Fourier transformed back to the time domain, removing any timing errors that would otherwise mix the absorptive and dispersive parts of the spectrum. The phase-corrected interferograms were apodized with a Hanning window and zero-padded to twice the number of points. Fourier transformation back to the frequency domain yielded a purely absorptive linear spectrum. The individual frequency-domain spectra were then averaged together. Transformed spectra with alternative windowing functions are given in Figure S2. Zero-padding by one or three times the number of points yields identical spectra. Averaging the time-domain interferograms together after phase correction and then Fourier transforming yield essentially identical frequency-domain spectra. Frequency-domain spectra obtained by truncating the time-domain signal at different delay times are identical except for the loss of spectral resolution (Figure S3), indicating that the only accessible dynamics is overall dephasing of the signal.

For the demonstration of a nonlinear signal, a zero-order CdSe half-wave plate (Alphalas; PO-TWP-L2−25-FIR) was placed in the fixed arm of the interferometer to rotate the polarization 90°. Assuming that rotational dynamics are negligible between pulses, the linear signal generated from two cross-polarized fields will orientationally average to zero. Since each individual pulse still contributes to the tag-loss signal, the nonlinear signal was measured by subtracting signal contributions from the individual pulses from the signal obtained with both pulses present: $S_{NL}(\tau) = S_{12}(\tau) - S_1 - S_2$. Measurements were performed at several delay times by successively measuring the average of each signal contribution over 500 mass spectrometry cycles at each delay. These experiments were performed 8 times over two different days. The average signals and error bars shown in Figure 4a come from these eight averages.

Frequency-Domain Experiments. A Nd:YAG laser (Amplitude Continuum Surelite EX, 10 Hz, 7 ns, 670 mJ/pulse) pumps an infrared optical parametric oscillator/amplifier (OPO/OPA) system (LaserVision). The output of the OPO/OPA spans 2000−4500 cm^{-1} with 2−40 mJ/pulse. The lower-frequency region (600−2200 cm^{-1}, 0.1−1 mJ/pulse) used in the experiments reported here is achieved through difference-frequency generation (DFG) of the OPA signal and idler outputs in $AgGaSe_2$ (Dien Tech). The bandwidth of the IR output is about 5 cm^{-1} in the lower-frequency region. The fluence is estimated to be $\sim 10^4$ μJ/cm^2 per pulse (1 mJ/pulse) with a pulse width of 7 ns. The intensity of the tag-loss photofragment was recorded as a function of laser frequency. The laser was scanned at 1.5 cm^{-1}/s between 1500 and 1900 cm^{-1}. Each spectrum was divided by the laser power spectrum to normalize for variation in laser power over the tuning range. The reported spectrum is the result of 16 averages, each binned by 1 cm^{-1}. Each spectrum took approximately 4 minutes to collect.

Computational. Structure optimization and harmonic frequency calculations of GlyGlyH$^+$ were performed with Guassian09[48] at the B3LYP/6-311++G(d,p) level of theory and basis set. The N_2 binding energy was computed to be ~1000 cm^{-1}. The H_2 binding energy was previously determined experimentally to be ~500 cm^{-1}.[38]

RESULTS

The interferogram of the ultrafast IR pulse pair, collected from the dark arm of the Mach−Zehnder interferometer, is displayed in Figure 2a. The IR source has sufficient bandwidth (Figure 3b; center frequency 1700 cm^{-1} and FWHM 260 cm^{-1}, as determined from a fit of the frequency-domain spectrum to a Gaussian function) to simultaneously excite the three dominant GlyGlyH$^+$ vibrational transitions in this region: the amide II mode at 1540 cm^{-1}, the amide I mode at 1725 cm^{-1}, and the C-terminus acid carbonyl stretch at 1785 cm^{-1}. The optimized structure, unscaled harmonic transitions, and normal mode displacement vectors are displayed in Figure 3a. We note that the original frequency-resolved studies of Johnson are consistent with the minimum-energy structure shown in Figure 3a being the only conformer present under these experimental conditions.[38]

The N_2 tag-loss action response as a function of the IR pulse pair delay time for a single data collection run is given in Figure 2b, while Figure 2c shows the average of all time-domain scans after phase correcting and normalizing each individual scan. The time-domain tag-loss signal displays high-frequency modulations around 20 fs, consistent with the oscillation periods of vibrational frequencies in this region. Lower-frequency components occurring at the relative frequencies between the vibrational transitions give rise to the beat pattern, with three main beats centered near τ = 0, 500, and 1000 fs and a weaker beat near 1500 fs emerging in the averaged signal.

A fit of the averaged interferogram in Figure 2c to a simple model equation

$$S(\tau) = \sum_{n=1}^{3} A_n \cos(\omega_{n0}\tau) e^{-\tau/T_2^{(n)}} \quad (1)$$

is shown in Figure 2d, where ω_{n0} are the fundamental vibrational frequencies of the three main transitions and $T_2^{(n)}$ are the phenomenological dephasing time constants for each

https://doi.org/10.1021/acs.jpca.1c01996
J. Phys. Chem. A 2021, 125, 10235−10244

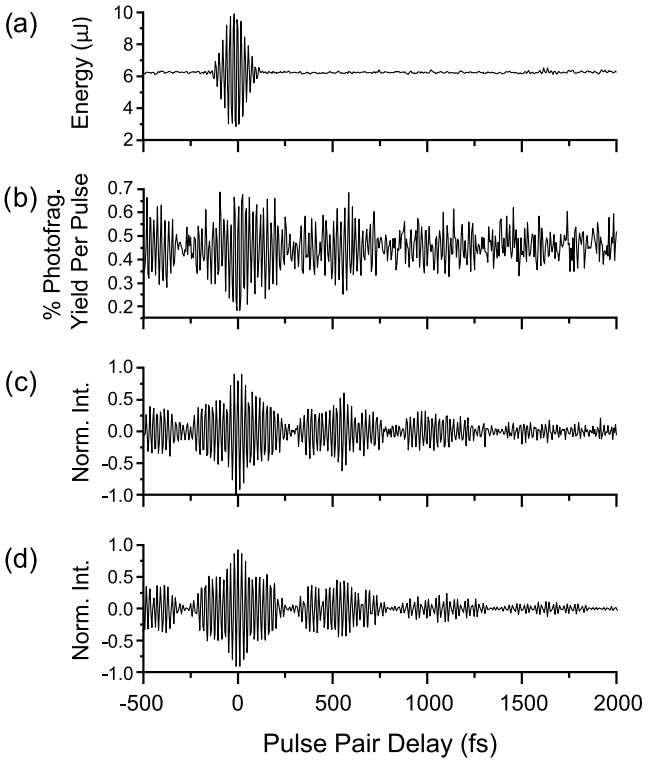

Figure 2. Time-domain $GlyGlyH^+$ N_2-tag loss as a function of the delay time between two replica ultrafast IR pulses. (a) Interferogram of the IR pulses. (b) N_2-tag-loss photofragmentation signal for a single representative data scan. (c) Average of the phase-corrected time-domain tag-loss interferograms showing interferences out to 1.5 ps. (d) Fit of the interferogram in panel (c) to eq 1 in the main text that models the signal as a superposition of three frequency components corresponding to the three dominant vibrational transition frequencies of $GlyGlyH^+$ in the spectral range spanned by the laser source.

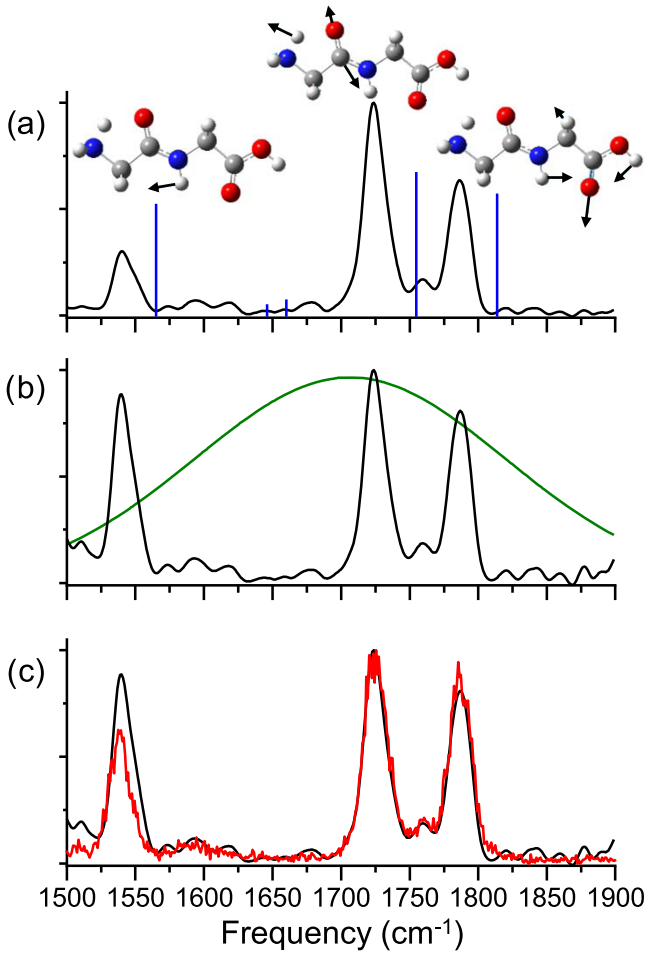

Figure 3. Frequency-domain cryogenic ion vibrational spectra of $GlyGlyH^+{\cdot}N_2$. (a) Averaged spectrum processed from the Fourier transformed time-domain signals collected with the ultrafast pulse pair. (b) Pump-normalized spectrum taken by dividing the spectrum in panel (a) by the laser spectrum (green). (c) Spectrum collected using the high-frequency-resolution IR source (red). The spectrum from (b) is overlaid in panel (c) for better comparison. The unscaled harmonic vibrational frequencies (blue sticks) and normal mode displacement vectors for the amide II (1540 cm^{-1}), amide I (1725 cm^{-1}), and acid carbonyl (1785 cm^{-1}) modes are shown in panel (a).

mode. The origin of eq 1 in the context of both time- and frequency-domain representations is discussed in more detail below. Equation 1 sufficiently captures the observed interference signal, with fitted vibrational frequencies of 1542(1) cm^{-1} (A_1 = 0.15(1)), 1724.3(3) cm^{-1} (A_2 = 0.53(1)), and 1786.9(5) cm^{-1} (A_3 = 0.33(1)). Dephasing times around 800 fs are obtained for each of the three modes: 860 ± 90, 810 ± 30, and 800 ± 40 fs for the amide II, amide I, and acid carbonyl modes, respectively. The complete set of fitting parameters and residuals are given in Figure S4. The fit to eq 1 demonstrates that the time-domain tag-loss signal can be satisfactorily described by the superposition of three components with frequencies matching those of the dominant $GlyGlyH^+$ vibrational transitions in the spectral range covered by the laser bandwidth.

To demonstrate that the time-domain experiments are monitoring the linear vibrational action spectrum, Figure 3 compares the frequency-domain spectrum obtained through the Fourier transform of the time-domain tag-loss interferograms to that measured using a high-frequency-resolution IR source in the standard CIVS approach. The averaged frequency-domain spectrum is shown in Figure 3a, while the spectrum in Figure 3b is normalized for the laser power by dividing the spectrum in 3a by the Gaussian fit of the laser spectrum (green trace in Figure 3b). The spectrum collected with the high-frequency-resolution IR source is shown in the red trace in Figure 3c (normalized by the laser power at each frequency) and is consistent with the spectrum collected by Johnson.[41] The laser-normalized trace from Figure 3b is overlaid in Figure 3c for a better comparison of the two methods. Importantly, the spectral frequencies and line widths obtained using the two methods are identical. The overlay shows that weaker spectral features are also captured in the time-domain experiment, in particular, the transition between the amide I and acid carbonyl modes at 1760 cm^{-1} (of unknown origin) and the broad transition(s) near 1600 cm^{-1} originating from NH_3^+ bending modes. The frequency-domain spectrum obtained from the time-domain data also appears to capture an asymmetry on the high-frequency side of the amide II transition, consistent with the observed shoulder in the frequency-domain experiment. Slight discrepancies in peak heights are attributed to the normalization schemes.

https://doi.org/10.1021/acs.jpca.1c01996
J. Phys. Chem. A 2021, 125, 10235−10244

DISCUSSION

Interpretations of the Time-Domain Signal. Action-detected interferometric measurements are most commonly discussed in the context of the wave-function-based first-order time-dependent perturbation theory.[8,9,49] In the weak-field limit, a single-photon process varies linearly with the excitation field such that the contributions from each field in a two-pulse sequence $E(t) = E_1(t) + E_2(t - \tau)$ can be treated separately and summed. Taking the initial population to be completely in the ground state, ϕ_0, the time-dependent wave function generated after interaction with the pulses can be expressed as

$$\psi(t) = \phi_0 + \sum_n \sum_p c_n^{(p)}(t)\phi_n \tag{2}$$

where p denotes the pulse number and n denotes the excited eigenstates (in our specific case, these will correspond to the three $GlyGlyH^+$ vibrational modes discussed above). The excited-state coefficients $c_n^{(p)}$ are given by

$$c_n^{(p)}(t) = \frac{-i}{\hbar} M_{n0} \int_0^\infty E_p(t - t') e^{i\omega_{n0}t'} dt' \tag{3}$$

where M_{n0} is the transition dipole moment. The observed action signal will be proportional to the total excited-state population after interaction with the two-pulse sequence $b(\tau)$

$$b(\tau) = \sum_n |c_n^{(1)}(t) + c_n^{(2)}(t - \tau)|^2$$
$$= \sum_n \frac{2|M_{n0}|^2 |E(\omega_{n0})|^2}{\hbar^2}(1 + \cos(\omega_{n0}\tau)) \tag{4}$$

The linear action response, therefore, manifests as an interferogram with a constant offset (resulting from interaction with pulse 1 or 2 only) and oscillatory components occurring at each transition frequency ω_{n0} (the v = 0−1 transition frequency of normal mode vibration n) arising from contributions due to both pulses. The modulation amplitude from each transition depends on the transition dipole moment squared, $|M_{n0}|^2$, and spectral amplitude of the pulses at each transition frequency, $|E(\omega_{n0})|^2$.

The expression can be interpreted as follows: the first pulse generates a coherent superposition state between v = 0 and 1 for each excited vibrational mode, which then evolve under the system Hamiltonian during the time delay τ between the two pulses. The excited coherences can undergo dephasing from both homogeneous and inhomogeneous dynamics that occur during the time delay between the pulses. Dephasing during the "coherence time" between pulses is typically accounted for using a phenomenological exponential decay term like the one introduced in eq 1.[1] The second pulse can also excite the system, generating a set of coherences that interfere with the first. Interference between the two possible, indistinguishable excitation pathways modulates the populations in v = 1 as a function of the delay time τ. The sum of the oscillatory terms from each excited transition will yield a beating pattern in the time domain described by the interferogram in eq 1.

In density matrix-based linear response formalism used to describe condensed-phase experiments,[1,50] a single laser pulse induces a macroscopic polarization in the sample that radiates a signal field. The signal field is the convolution of the excitation field, with the field emitted by the excited coherences as described by the linear response function: $R^{(1)}(t) \propto |M_{n0}|^2 e^{i\omega_{n0}t} e^{-t/T_2}$. The convolution (interference) between these fields, either in the time domain using a pulse pair[51] or in the frequency domain using a spectrometer,[1] allows for the extraction of the molecular information contained in the linear response function: the linear absorption spectrum of the system. In the action-based experiments performed here, the observed interference signal described by eqs 1 and 4 can be viewed as an indirect measurement of the linear response function.

It is important to emphasize that the above expressions and interpretations do not depend on the time duration or shape of the initial pulse and only require that the two pulses are coherent with respect to each other.[49,52] That is, a linear spectrum is independent of the phase relationships between the different frequency components contained in the light pulse. Ultrafast pulses do not provide any additional information compared to nonphase-locked pulses or frequency-domain approaches in linear spectroscopy. Indeed, coherent oscillatory signals can be observed when using spectrally incoherent light[51,53] since time resolution depends on the temporal coherence length (given by the autocorrelation function $\langle E(t)E(t - \tau)\rangle$) and not the temporal envelope of the pulse. Coherent oscillatory signals have also been measured in experiments using frequency-comb sources.[52,54] For time-domain linear spectroscopy, the main benefit of ultrafast pulses is the simplified mathematical treatment and interpretation when in the impulsive limit; the measured signals are directly proportional to the linear response function, which contains the desired molecular information, and not the convolution with the excitation field.

There is a complementary frequency-domain picture when considering the total field $E(t)$. The power spectrum of a replica pulse pair $E(t) = E_1(t) + E_2(t - \tau)$ is a cosine-modulated amplitude spectrum in the frequency domain

$$|E(\omega)|^2 = 2|E_1(\omega)|^2(1 + \cos(\omega\tau)) \tag{5}$$

Note that eq 5 yields the same result as eq 4. Therefore, one can consider the experiment in terms of light interference (spectral amplitude modulation) in the frequency domain. For the experiments performed here, when the near-transform-limited pulses are overlapped well within the temporal coherence length, the observed signal is best described in terms of the frequency modulations described by eq 5. When the pulses are well separated temporally, however, we believe the coherence interference picture is a more accurate description of the experiment. Although eq 5 predicts light interference beyond the temporal coherence length, this interference resides solely in the frequency domain. Interference in this regime is observable when using, for example, a spectrometer to separate out the frequency components contained in the pulse, thus increasing the coherence lengths of each frequency component and allowing interference to occur in space.[49,55,56]

Outlook for 2D IR Spectroscopy of Trapped Molecular Ions. Given the weak linear action signals per pulse observed using the ultrafast IR source, we must assess the prospects of measuring even weaker nonlinear signals. For a single arm of the IR pulse pair, about 35% photofragmentation yield is observed after excitation of the trapped ions with ~80 pulses. This is a photofragmentation yield per pulse of about 0.4% (Figure 2b), assuming that the total number of ions excited within the ensemble is small enough to be considered approximately the same per pulse. Assuming photofragmentation results from successful absorption of a single photon, this

https://doi.org/10.1021/acs.jpca.1c01996
J. Phys. Chem. A 2021, 125, 10235−10244

indicates that the probability of excitation, equal to the total excited-state population, is about 0.4%. As detailed in the Supporting Information, using the calculated transition dipole moments and measured intensity of the pulse, the predicted excitation probability for each of the three dominant $GlyGlyH^+$ transitions in the region studied is about 0.1%. This gives a total probability of excitation of about 0.3% per pulse, in close agreement with the observed photofragmentation yield.

Nonlinear pump−probe and 2D signals for fundamental transitions will scale as $|M_{10}|^4$. Based on the single-pulse excitation probabilities, signal pathways expected from nonlinear response theory, and orientational factors, we anticipate a nonlinear pump−probe photofragmentation signal deriving from the fundamental transitions (excluding cross peaks) on the order of 10^{-3}% per pulse. For the full 80 pulse cycle on the experiment, this corresponds to a predicted total measured signal of about 0.1%. This total signal level is below the detection limit of ∼2% and the shot-to-shot fluctuations in the background linear signal of ∼10%.

To see if the nonlinear signal were present and detectable under the current conditions, we monitored photofragmentation using a cross-polarized pulse pair. This arrangement eliminates the background linear response that arises from the interaction of both pulses together through the orientational averaging of the excited dipoles, assuming rotational motion is negligible over the time scale between pulses (computed rotational A constant of 5 GHz, corresponding to a rotational period of about 200 ps). Linear signal deriving from interactions with each pulse individually, however, still remains. To isolate the nonlinear response, we subtracted the photofragmentation signal resulting from each individual pulse from the photofragmentation measured with both pulses present. The total nonlinear photofragmentation signal measured at several waiting times between pump and probe pulses is shown in Figure 4a. Encouragingly, we obtained a measurable nonlinear signal with values (∼0.05−0.1% per pulse) larger than anticipated and overall negative.

The possible pathways that contribute to a nonlinear pump−probe signal due to single interactions with pump and probe, excluding cross peaks, are depicted in the energy level diagrams in Figure 4b. Signals that occur at the fundamental frequencies ω_{10} derive from ground-state bleaching (GSB) and stimulated emission (SE) pathways. These signals are negative since the presence of the pump reduces the total excited-state population induced by the probe. There is also an excited-state absorption (ESA) contribution at frequency ω_{21} due to excitation between the v = 1 and v = 2 levels. The ESA yields a positive signal since this excitation pathway is not present in the absence of the pump. Since $M_{21} = \sqrt{2}M_{10}$ for a harmonic oscillator, the total nonlinear signal should ideally be zero, at least at the earliest waiting times. This is also true in condensed-phase pump−probe or 2D IR experiments. The observed negative signal could result from the fact that ESA transitions decay faster than bleach signals since the population in v = 1 will relax through background bath states and not directly back to the ground state. Therefore, as waiting time increases, the contribution from negative bleach signals will increase relative to the positive ESA responses. The observed signal is in line with this expectation when considering the anticipated vibrational lifetimes of <1 ps based on the line widths and dephasing times for the transitions interrogated.

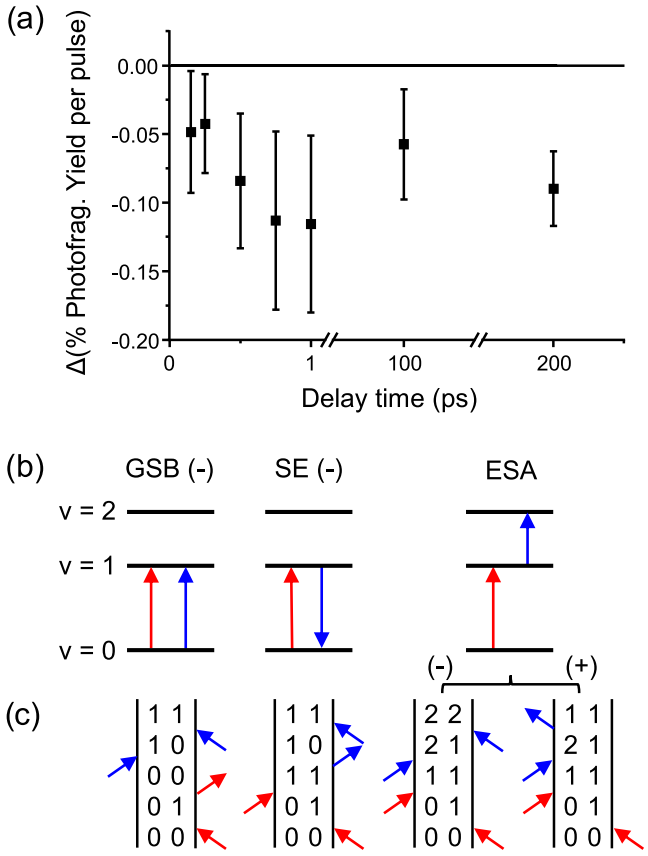

Figure 4. (a) Total nonlinear photofragmentation signal measured using cross-polarized pump and probe pulses. The nonlinear signal was measured by subtracting the photofragmentation observed from each individual pulse from that when both pulses were present. The signal was not frequency-resolved. (b) Energy level diagram for a single oscillator indicating possible nonlinear signal pathways for single interactions with pump (red) and probe (blue) pulses. (c) Rephasing Feynman diagram pathways expected from nonlinear response formalism due to two simultaneous interactions each with the pump and probe pulses. Negative nonlinear signals result from ground-state bleaching (GSB), stimulated emission (SE), and one excited-state absorption (ESA) pathway. Positive nonlinear signals derive from an additional ESA pathway. Each signal contribution will have an additional nonrephasing pathway.

Alternatively, action-based nonlinear experiments have been described using density matrix nonlinear response formalism, even in dilute gas-phase systems, where the pump and probe pulses each formally provide two simultaneous interactions with the system.[10,13,57,58] The fourth and final interaction places the system into an excited population state, which is read out by the action response. Unlike condensed-phase nonlinear experiments that have three formal field interactions, the action-based four-field scheme results in an additional ESA contribution at ω_{21} corresponding to bleaching of the v = 1 level.[57,59] For a harmonic oscillator, these two ESA pathways will cancel leaving only GSB and SE pathways to contribute to the nonlinear signal. This perspective could also be used to explain the presence of a negative nonlinear signal even at the earliest waiting times. Feynman diagrams for the four possible rephasing pathways under nonlinear response formalism are shown in Figure 4c.

We have not taken into account possible cross peaks that are undoubtedly present among the three strongly coupled

https://doi.org/10.1021/acs.jpca.1c01996
J. Phys. Chem. A 2021, 125, 10235−10244

$GlyGlyH^+$ modes excited by the pump nor the weaker transitions near 1600 and 1760 cm^{-1} observed in the linear spectrum. These additional contributions could account for the larger than expected overall magnitude of the nonlinear signal, particularly if ESA pathways do indeed cancel. Further, the general increase in the nonlinear bleaching signal between 150 fs (earliest time that ensures no pulse overlap) and 1 ps could arise from growing cross-peak contributions. Interestingly, we observe a persistent bleach signal at 100 and 200 ps. This suggests that either tag loss has not yet occurred on these time scales or that tag loss induced by the first pulse is sufficiently large to eliminate a measurable portion of tagged ions seen by the probe at these long delay times. The former is an interesting prospect as tag loss occurring on relatively long time scales would not hinder the measurement of the desired system dynamics.

Frequency-resolving the nonlinear signal into a pump−probe or 2D spectrum is likely not possible at the current signal-to-noise levels. The fluence of the ultrafast pulses is quite low in the current design due to soft focusing of the beams into the ion trap. A tighter focus would help enhance the nonlinear signal. The signal can also be increased by increasing the number of trapped ions. Although ion density is quite limited in a 3D Paul trap, a linear trap can be employed with excitation along the longitudinal axis of the trap. The messenger-tagging method also presents many complications: tag-loss background signal from each pulse, tag-loss dynamics, and much weaker signal compared to the untagged species. These issues could be addressed by monitoring, for example, the photofragmentation of untagged ions using a fifth pulse (multiphoton UV−vis or 800 nm) as the action response in a similar scheme to Stienkemeier, which was also shown to enhance the positive ESA pathway.[12] Moving forward, we believe that the best approach will be to use a pulse shaper to generate a set of four collinear pulses whose phases can be modulated to generate a series of sequences that can be used to isolate the desired nonlinear response from the background linear signals.[10−13] Stienkemeier has also demonstrated that the Fourier transform of time-domain interferograms collected using phase modulation and rotating frame sampling yield frequency-domain spectra with much improved signal to noise.[60]

CONCLUSIONS

We have demonstrated an important and necessary prerequisite step toward the implementation of time-resolved multidimensional vibrational spectroscopy of gaseous molecular ions by showing that excited-state vibrational populations modulated by an ultrafast IR pulse pair are mapped onto messenger tag photodissociation and can be used to extract the linear frequency-domain spectrum. Critically, we have also shown that nonlinear pump−probe signals are measurable under the current experimental conditions. The next crucial step is to introduce a probe pulse pair[57] in the pump−probe scheme used to collect the nonlinear data presented in Figure 4a to frequency-resolve the bleach and (possibly) ESA transitions and to monitor their time evolution with a pump−probe delay time. The collection of a 2D spectrum will require an additional pump pulse pair. In an overly simplified perspective, a 2D spectrum can be obtained through a 2D Fourier transform of the action signal response as a function of two delay times: that between a pump pulse pair and that between a probe pulse pair.

A challenging question that remains is to what extent tag loss contributes to the decay of the observed time-domain signal. The mechanism of tag loss is usually described in the context of intramolecular vibrational redistribution (IVR) where the vibrational relaxation of the excited oscillators to low-frequency modes, particularly ion-tag soft modes, via anharmonic coupling leads to photodissociation.[61,62] The tag-loss dynamics, therefore, are intimately related to the population relaxation component (T_1) of the dephasing time. In an ideal scenario, the decay would be purely from dephasing and tag loss would occur on much longer time scales (tens of picoseconds or longer) such that the measured dynamics are not influenced or limited by the tag-loss process. The initial nonlinear data presented in Figure 4a is promising in this regard. We hope the future demonstration of time-resolved and multidimensional spectra of well-defined, isolated ionic systems with diverse chemical complexity will foster fruitful collaborations between the gas-phase and condensed-phase communities.

ASSOCIATED CONTENT

Supporting Information

The Supporting Information is available free of charge at https://pubs.acs.org/doi/10.1021/acs.jpca.1c01996.

> Power dependence of the time- and frequency-domain signals obtained with the ultrafast pulse pair (Figure S1); Fourier transformed spectrum using different windowing functions (Figure S2); Fourier transformed spectra after truncating the time-domain signal at various delay times (Figure S3); fit of eq 1 to the averaged time-domain data (Figure S4); and calculations predicting linear and nonlinear photofragmentation signals (PDF)

AUTHOR INFORMATION

Corresponding Author

Joseph A. Fournier − *Department of Chemistry, Washington University in St. Louis, St. Louis, Missouri 63130, United States*; orcid.org/0000-0001-7569-9176; Email: jfournier@wustl.edu

Authors

Liangyi Chen − *Department of Chemistry, Washington University in St. Louis, St. Louis, Missouri 63130, United States*

Jessika L. S. Dean − *Department of Chemistry, Washington University in St. Louis, St. Louis, Missouri 63130, United States*

Complete contact information is available at: https://pubs.acs.org/10.1021/acs.jpca.1c01996

Notes

The authors declare no competing financial interest.

ACKNOWLEDGMENTS

The authors gratefully acknowledge the National Science Foundation for support through a CAREER Award (grant number CHE-2044927) and Washington University in St. Louis and the Department of Chemistry for generous start-up funding.

REFERENCES

(1) Hamm, P.; Zanni, M. T., *Concepts and Methods of 2D Infrared Spectroscopy*. Cambridge UP: Cambridge, 2011.

(2) Khalil, M.; Demirdoven, N.; Tokmakoff, A. Coherent 2D IR Spectroscopy: Molecular Structure and Dynamics in Solution. *J. Phys. Chem. A* **2003**, *107*, 5258−5279.

(3) Hybl, J. D.; Albrecht, A. W.; Faeder, S. M. G.; Jonas, D. M. Two-Dimensional Electronic Spectroscopy. *Chem. Phys. Lett.* **1998**, *297*, 307−313.

(4) Hybl, J. D.; Ferro, A. A.; Jonas, D. M. Two-Dimensional Fourier Transform Electronic Spectroscopy. *J. Chem. Phys.* **2001**, *115*, 6606−6622.

(5) Hamm, P.; Shalit, A. Perspective: Echoes in 2D-Raman-THz Spectroscopy. *J. Chem. Phys.* **2017**, *146*, No. 130901.

(6) Courtney, T. L.; Fox, Z. W.; Estergreen, L.; Khalil, M. Measuring Coherently Coupled Intramolecular Vibrational and Charge-Transfer Dynamics with Two-Dimensional Vibrational Electronic Spectroscopy. *J. Phys. Chem. Lett.* **2015**, *6*, 1286−1292.

(7) Oliver, T. A. A.; Lewis, N. H. C.; Fleming, G. R. Correlating the Motion of Electrons and Nuclei with Two-Dimensional Electronic-Vibrational Spectroscopy. *Proc. Natl. Acad. Sci. U.S.A.* **2014**, *111*, 10061−10066.

(8) Scherer, N. F.; Carlson, R. J.; Matro, A.; Du, M.; Ruggiero, A. J.; Romerorochin, V.; Cina, J. A.; Fleming, G. R.; Rice, S. A. Fluorescence-Detected Wave Packet Interferometry - Time Resolved Molecular-Spectroscopy with Sequences of Femtosecond Phase-Locked Pulses. *J. Chem. Phys.* **1991**, *95*, 1487−1511.

(9) Tekavec, P. F.; Dyke, T. R.; Marcus, A. H. Wave Packet Interferometry and Quantum State Reconstruction by Acousto-Optic Phase Modulation. *J. Chem. Phys.* **2006**, *125*, No. 194303.

(10) Tekavec, P. F.; Lott, G. A.; Marcus, A. H. Fluorescence-Detected Two-Dimensional Electronic Coherence Spectroscopy by Acousto-Optic Phase Modulation. *J. Chem. Phys.* **2007**, *127*, No. 214307.

(11) Roeding, S.; Brixner, T. Coherent Two-Dimensional Electronic Mass Spectrometry. *Nat. Commun.* **2018**, *9*, No. 2519.

(12) Bruder, L.; Bangert, U.; Binz, M.; Uhl, D.; Vexiau, R.; Bouloufa-Maafa, N.; Dulieu, O.; Stienkemeier, F. Coherent Multidimensional Spectroscopy of Dilute Gas-Phase Nanosystems. *Nat. Commun.* **2018**, *9*, No. 4823.

(13) Bruder, L.; Bangert, U.; Binz, M.; Uhl, D.; Stienkemeier, F. Coherent Multidimensional Spectroscopy in the Gas Phase. *J. Phys. B: At., Mol. Opt. Phys.* **2019**, *52*, No. 183501.

(14) Nardin, G.; Autry, T. M.; Silverman, K. L.; Cundiff, S. T. Multidimensional Coherent Photocurrent Spectroscopy of a Semiconductor Nanostructure. *Opt. Express* **2013**, *21*, 28617−28627.

(15) Liebel, M.; Toninelli, C.; van Hulst, N. F. Room-Temperature Ultrafast Nonlinear Spectroscopy of a Single Molecule. *Nat. Photonics* **2018**, *12*, 45−49.

(16) Reber, M. A. R.; Chen, Y. N.; Allison, T. K. Cavity-Enhanced Ultrafast Spectroscopy: Ultrafast Meets Ultrasensitive. *Optica* **2016**, *3*, 311−317.

(17) Silfies, M. C.; Kowzan, G.; Lewisa, N.; Allison, T. K. Broadband Cavity-Enhanced Ultrafast Spectroscopy. *Phys. Chem. Chem. Phys.* **2021**, *23*, 9743−9752.

(18) Garand, E.; Kamrath, M. Z.; Jordan, P. A.; Wolk, A. B.; Leavitt, C. M.; McCoy, A. B.; Miller, S. J.; Johnson, M. A. Determination of Noncovalent Docking by Infrared Spectroscopy of Cold Gas-Phase Complexes. *Science* **2012**, *335*, 694−698.

(19) Perez, E. H.; Menges, F. S.; Cattaneo, M.; Mayer, J. M.; Johnson, M. A. Characterization of the Non-Covalent Docking Motif in the Isolated Reactant Complex of a Double Proton-Coupled Electron Transfer Reaction with Cryogenic Ion Spectroscopy. *J. Chem. Phys.* **2020**, *152*, No. 234309.

(20) Nosenko, Y.; Menges, F.; Riehn, C.; Niedner-Schatteburg, G. Investigation by Two-Color IR Dissociation Spectroscopy of Hoogsteen-Type Binding in a Metalated Nucleobase Pair Mimic. *Phys. Chem. Chem. Phys.* **2013**, *15*, 8171−8178.

(21) Duffy, E. M.; Voss, J. M.; Garand, E. Vibrational Characterization of Microsolvated Electrocatalytic Water Oxidation Intermediate: $Ru(tpy)(bpy)(OH)^{2+}(H_2O)_{0-4}$. *J. Phys. Chem. A* **2017**, *121*, 5468−5474.

(22) Knurr, B. J.; Weber, J. M. Solvent-Driven Reductive Activation of Carbon Dioxide by Gold Anions. *J. Am. Chem. Soc.* **2012**, *134*, 18804−18808.

(23) Ricks, A. M.; Brathwaite, A. D.; Duncan, M. A. Ir Spectroscopy of Gas Phase $V(CO_2)_n^+$ Clusters: Solvation-Induced Electron Transfer and Activation of CO_2. *J. Phys. Chem. A* **2013**, *117*, 11490−11498.

(24) Munshi, M. U.; Craig, S. M.; Berden, G.; Martens, J.; DeBlase, A. F.; Foreman, D. J.; McLuckey, S. A.; Oomens, J.; Johnson, M. A. Preparation of Labile Ni^+(cyclam) Cations in the Gas Phase Using Electron-Transfer Reduction through Ion-Ion Recombination in an Ion Trap and Structural Characterization with Vibrational Spectroscopy. *J. Phys. Chem. Lett.* **2017**, *8*, 5047−5052.

(25) Cirri, A.; Hernndez, H. M.; Kmiotek, C.; Johnson, C. J. Systematically Tuning the Electronic Structure of Gold Nanoclusters through Ligand Derivatization. *Angew. Chem., Int. Ed.* **2019**, *58*, 13818−13822.

(26) Fournier, J. A.; Wolke, C. T.; Johnson, M. A.; Odbadrakh, T. T.; Jordan, K. D.; Kathmann, S. M.; Xantheas, S. S. Snapshots of Proton Accommodation at a Microscopic Water Surface: Understanding the Vibrational Spectral Signatures of the Charge Defect in Cryogenically Cooled $H^+(H_2O)_{n=2-28}$ Clusters. *J. Phys. Chem. A* **2015**, *119*, 9425−9440.

(27) Heine, N.; Fagiani, M. R.; Asmis, K. R. Disentangling the Contribution of Multiple Isomers to the Infrared Spectrum of the Protonated Water Heptamer. *J. Phys. Chem. Lett.* **2015**, *6*, 2298−2304.

(28) Mizuse, K.; Mikami, N.; Fujii, A. Infrared Spectra and Hydrogen-Bonded Network Structures of Large Protonated Water Clusters $H^+(H_2O)_n$ (n=20−200). *Angew. Chem., Int. Ed.* **2010**, *49*, 10119−10122.

(29) Goebbert, D. J.; Garand, E.; Wende, T.; Bergmann, R.; Meijer, G.; Asmis, K. R.; Neumark, D. M. Infrared Spectroscopy of the Microhydrated Nitrate Ions $NO_3^-(H_2O)_{1-6}$. *J. Phys. Chem. A* **2009**, *113*, 7584−7592.

(30) Heine, N.; Asmis, K. R. Cryogenic Ion Trap Vibrational Spectroscopy of Hydrogen-Bonded Clusters Relevant to Atmospheric Chemistry. *Int. Rev. Phys. Chem.* **2015**, *34*, 1−34.

(31) Kreinbihl, J. J.; Frederiks, N. C.; Waller, S. E.; Yang, Y.; Johnson, C. J. Establishing the Structural Motifs Present in Small Ammonium and Aminium Bisulfate Clusters of Relevance to Atmospheric New Particle Formation. *J. Chem. Phys.* **2020**, *153*, No. 034307.

(32) Okumura, M.; Yeh, L. I.; Myers, J. D.; Lee, Y. T. Infrared Spectra of the Cluster Ions $H_7O_3^+ \cdot H_2$ and $H_9O_4^+ \cdot H_2$. *J. Chem. Phys.* **1986**, *85*, 2328−2329.

(33) Marsh, B. M.; Voss, J. M.; Garand, E. A Dual Cryogenic Ion Trap Spectrometer for the Formation and Characterization of Solvated Ionic Clusters. *J. Chem. Phys.* **2015**, *143*, No. 204201.

(34) Kreinbihl, J. J.; Frederiks, N. C.; Johnson, C. J. Hydration Motifs of Ammonium Bisulfate Clusters Show Complex Temperature Dependence. *J. Chem. Phys.* **2021**, *154*, No. 014304.

(35) Robertson, W. H.; Kelley, J. A.; Johnson, M. A. A Pulsed Supersonic Entrainment Reactor for the Rational Preparation of Cold Ionic Complexes. *Rev. Sci. Instrum.* **2000**, *71*, 4431−4434.

(36) Wolk, A. B.; Leavitt, C. M.; Garand, E.; Johnson, M. A. Cryogenic Ion Chemistry and Spectroscopy. *Acc. Chem. Res.* **2014**, *47*, 202−210.

(37) Garand, E. Spectroscopy of Reactive Complexes and Solvated Clusters: A Bottom-Up Approach Using Cryogenic Ion Traps. *J. Phys. Chem. A* **2018**, *122*, 6479−6490.

(38) Kamrath, M. Z.; Garand, E.; Jordan, P. A.; Leavitt, C. M.; Wolk, A. B.; Van Stipdonk, M. J.; Miller, S. J.; Johnson, M. A. Vibrational Characterization of Simple Peptides Using Cryogenic Infrared Photodissociation of H2-Tagged, Mass-Selected Ions. *J. Am. Chem. Soc.* **2011**, *133*, 6440−6448.

https://doi.org/10.1021/acs.jpca.1c01996
J. Phys. Chem. A 2021, 125, 10235−10244

(39) Leavitt, C. M.; Wolk, A. B.; Kamrath, M. Z.; Garand, E.; Van Stipdonk, M. J.; Johnson, M. A. Characterizing the Intramolecular H-Bond and Secondary Structure in Methylated GlyGlyH$^+$ with H_2 Predissociation Spectroscopy. *J. Am. Soc. Mass Spectrom.* **2011**, *22*, 1941−1952.
(40) Leavitt, C. M.; Wolk, A. B.; Fournier, J. A.; Kamrath, M. Z.; Garand, E.; Van Stipdonk, M. J.; Johnson, M. A. Isomer-Specific IR-IR Double Resonance Spectroscopy of D2-Tagged Protonated Dipeptides Prepared in a Cryogenic Ion Trap. *J. Phys. Chem. Lett.* **2012**, *3*, 1099−1105.
(41) Leavitt, C. M.; Deblase, A. F.; Johnson, C. J.; Van Stipdonk, M.; McCoy, A. B.; Johnson, M. A. Hiding in Plain Sight: Unmasking the Diffuse Spectral Signatures of the Protonated N-Terminus in Isolated Dipeptides Cooled in a Cryogenic Ion Trap. *J. Phys. Chem. Lett.* **2013**, *4*, 3450−3457.
(42) Kamrath, M. Z.; Relph, R. A.; Guasco, T. L.; Leavitt, C. M.; Johnson, M. A. Vibrational Predissociation Spectroscopy of the H_2-Tagged Mono- and Dicarboxylate Anions of Dodecanedioic Acid. *Int. J. Mass Spectrom.* **2011**, *300*, 91−98.
(43) Marsh, B. M.; Zhou, J.; Garand, E. Vibrational Spectroscopy of Small Hydrated CuOH$^+$ Clusters. *J. Phys. Chem. A* **2014**, *118*, 2063−2071.
(44) Parks, J. H.; Szoke, A. Simulation of Collisional Relaxation of Trapped Ion Clouds in the Presence of Space-Charge Fields. *J. Chem. Phys.* **1995**, *103*, 1422−1439.
(45) Yang, N.; Edington, S. C.; Choi, T. H.; Henderson, E. V.; Heindel, J. P.; Xantheas, S. S.; Jordan, K. D.; Johnson, M. A. Mapping the Temperature-Dependent and Network Site-Specific Onset of Spectral Diffusion at the Surface of a Water Cluster Cage. *Proc. Natl. Acad. Sci. U.S.A.* **2020**, *117*, 26047−26052.
(46) Kaindl, R. A.; Wurm, M.; Reimann, K.; Hamm, P.; Weiner, A. M.; Woerner, M. Generation, Shaping, and Characterization of Intense Femtosecond Pulses Tunable from 3 to 20 μm. *J. Opt. Soc. Am. B* **2000**, *17*, 2086−2094.
(47) Mertz, L. Auxiliary Computation for Fourier Spectrometry. *Infrared Phys.* **1967**, *7*, 17−23.
(48) Frisch, M. J.; Trucks, G. W.; Schlegel, H. B.; Scuseria, G. E.; Robb, M. A.; Cheeseman, J. R.; Scalmani, G.; Barone, V.; Mennucci, B.; Petersson, G. A. et al. *Gaussian 09*, revision D.01; Gaussian, Inc.: Wallingford, CT, 2009.
(49) Bouchene, M. A.; Blanchet, V.; Nicole, C.; Melikechi, N.; Girard, B.; Ruppe, H.; Rutz, S.; Schreiber, E.; Woste, L. Temporal Coherent Control Induced by Wave Packet Interferences in One and Two Photon Atomic Transitions. *Eur. Phys. J. D: At., Mol. Opt. Phys.* **1998**, *2*, 131−141.
(50) Mukamel, S. *Principles of Nonlinear Optical Spectroscopy*; Oxford University Press: New York, 1995.
(51) Turner, D. B.; Arpin, P. C.; McClure, S. D.; Ulness, D. J.; Scholes, G. D. Coherent Multidimensional Optical Spectra Measured Using Incoherent Light. *Nat. Commun.* **2013**, *4*, No. 2298.
(52) Witte, S.; Zinkstok, R. T.; Ubachs, W.; Hogervorst, W.; Eikema, K. S. E. Deep-Ultraviolet Quantum Interference Metrology with Ultrashort Laser Pulses. *Science* **2005**, *307*, 400−403.
(53) Jones, R. R.; Schumacher, D. W.; Gallagher, T. F.; Bucksbaum, P. H. Bound-State Interferometry Using Incoherent Light. *J. Phys. B: At., Mol. Opt. Phys.* **1995**, *28*, L405−L411.
(54) Morgenweg, J.; Barmes, I.; Eikema, K. S. E. Ramsey-Comb Spectroscopy with Intense Ultrashort Laser Pulses. *Nat. Phys.* **2014**, *10*, 30−33.
(55) Hikosaka, Y.; Kaneyasu, T.; Fujimoto, M.; Iwayama, H.; Katoh, M. Reply to 'Comment on "Coherent Control in the Extreme Ultraviolet and Attosecond Regime by Synchrotron Radiation"'. *Nat. Commun.* **2021**, *12*, No. 3782.
(56) Devrelis, V.; Oconnor, M.; Munch, J. Coherence Length of a Single Laser-Pulse as Measured by CCD Interferometry. *Appl. Optics* **1995**, *34*, 5386−5389.
(57) Malý, P.; Brixner, T. Fluorescence-Detected Pump-Probe Spectroscopy. *Angew. Chem., Int. Ed.* **2021**, *60*, 18867−18875.
(58) Grimberg, B. I.; Lozovoy, V. V.; Dantus, M.; Mukamel, S. Ultrafast Nonlinear Spectroscopic Techniques in the Gas Phase and Their Density Matrix Representation. *J. Phys. Chem. A* **2002**, *106*, 697−718.
(59) Perdomo-Ortiz, A.; Widom, J. R.; Lott, G. A.; Aspuru-Guzik, A.; Marcus, A. H. Conformation and Electronic Population Transfer in Membrane-Supported Self-Assembled Porphyrin Dimers by 2D Fluorescence Spectroscopy. *J. Phys. Chem. B* **2012**, *116*, 10757−10770.
(60) Bruder, L.; Mudrich, M.; Stienkemeier, F. Phase-Modulated Electronic Wave Packet Interferometry Reveals High Resolution Spectra of Free Rb Atoms and Rb*He Molecules. *Phys. Chem. Chem. Phys.* **2015**, *17*, 23877−23885.
(61) Nesbitt, D. J.; Field, R. W. Vibrational Energy Flow in Highly Excited Molecules: Role of Intramolecular Vibrational Redistribution. *J. Phys. Chem. A.* **1996**, *100*, 12735−12756.
(62) Gruebele, M.; Wolynes, P. G. Vibrational Energy Flow and Chemical Reactions. *Acc. Chem. Res.* **2004**, *37*, 261−267.

https://doi.org/10.1021/acs.jpca.1c01996
J. Phys. Chem. A 2021, 125, 10235−10244